Water as Additive Directing Lithium Electrodeposition

Mark Aarts[a,b,*], Sai Gourang Patnaik[a,b], Toon Van Roy[a,b], Stefanie Sergeant[c], Maarten Debucquoy[a,b], Philippe M. Vereecken[a,d,b,*]

[a] imec, Energy Department, Kapeldreef 75, 3001 Leuven, Belgium

[b] Energyville, Thor Park 8310, 3600, Genk, Belgium

[c] imec, Department of Material and Component Analysis, Kapeldreef 75, 3001 Leuven, Belgium

[d] KU Leuven, Department of Microbial and Micromolecular systems (M2S), cMACS, Celestijnenlaan 200F, 3001 Leuven, Belgium

[*] m.aarts@lic.leidenuniv.nl, Philippe.Vereecken@imec.be

Abstract

Electroplating of flat lithium layers is key for batteries using metallic lithium as the anode. For this, an intriguing growth mode is a self-assembled, compact, columnar morphology of electrodeposited lithium. Here, we demonstrate the electrodeposition of columnar lithium from LiTFSI and $LiClO_4$ salts using water as additive, excluding commonly found explanations of LiF directing growth. We independently investigate the effect of water during electrochemical formation and growth, showing that it is required continuously. The process is studied *in-situ* using a rotating ring-disk-electrode (RRDE). We observe a dynamic passivation process, attributed to the continuous formation/dissolution of LiOH and Li_2O surface layers, accompanied by H_2 evolution and likely LiH formation. Notably, hydrogen is produced in the LiF-based mechanism, suggesting it to be an integral component for directing growth. This homogenizes our results with literature, providing mechanistic insights on the role of water for the design of electrodeposited lithium morphologies and surface chemistry.

Control over the morphology of lithium metal during electrodeposition has become a major topic in battery research[1,2], with many works focusing on the stability of the lithium metal anode over repeated electroplating and stripping cycles[3–6]. Cycling and subsequent observation, typically using scanning electron microscopy (SEM), does not always provide the full picture however, as illustrated in literature by recent mechanistic insights obtained using a variety of additional techniques to study lithium metal growth[7–13]. Furthermore, the wide range of electrolyte systems makes it difficult to compare results[14], or to disentangle physical[15] and chemical[16] effects responsible for uncontrolled lithium growth. Growth of smooth lithium attributed to electrostatic shielding for example[17], was later found to consist of a particular self-aligned and compact nanorod morphology[18].

Such a columnar morphology is very similar to the results first obtained by Kanamura et al.[19] using an HF additive, and later with trace amounts of water for the *in-situ* formation of HF through hydrolysis of a $LiPF_6$ electrolyte[20]. This growth mode is commonly attributed to a LiF solid electrolyte interphase (SEI) layer, mainly through X-ray photoelectron spectroscopy (XPS)[21–23]. So far, deposition of columnar lithium layers has attracted interest for its smooth or 'dendrite-free' morphology, but has also shown improved results in terms of lifetime[24] and Coulombic efficiency[25]. In particular, a unique plating and stripping along the length of the columns was observed in cycling[18,26,27] implying reduced local current densities and limited

volumetric change of the lithium metal anode, mitigating well-known causes of ramified growth and failure in lithium metal batteries.

Recently however, questions have been raised about the role of LiF[28], with similar structures also being observed in (non-hydrolyzing) LiTFSI[23] and $LiNO_3$[29] electrolytes. As the bulk of the aforementioned references advocate formation of a LiF-rich SEI through the electrocatalytic reduction of HF as the cause for columnar growth, a more complete understanding of the responsible mechanism is required for further optimization.

In this work we demonstrate the electrodeposition of columnar lithium morphologies obtained directly with water as additive. We achieve these using both non-hydrolyzing LiTFSI, and fluorine-free $LiClO_4$ electrolytes, unambiguously proving that a LiF-rich SEI cannot be considered as the sole determining factor for this growth mode. We investigate the role of the formation step (i.e. electrochemical reactions occurring at potentials above the lithium deposition potential) using *ex-situ* glovebox Atomic Force Microscopy (AFM), and electrochemical experiments. No templating layer is observed to account for our experimental results, and the water is shown to have a continuous role during growth. Finally, we use a rotating ring-disk-electrode (RRDE) to study the growth process *in-situ.* We observe a dynamic passivation of the layer during growth. This is attributed to the continuous formation/dissolution of LiOH and Li_2O surface layers, accompanied by H_2 evolution and likely LiH formation. Notably, hydrogen is also reported as a product during electrocatalytic formation of LiF in electrolytes containing HF, suggesting it to be an integral component for the directed growth. Such an explanation homogenizes our results with existing literature and provides mechanistic insights for the design and control of lithium metal morphologies and surface chemistries.

Columnar lithium electrodeposition

Lithium electrodeposition was carried out in a 3-electrode cell using a copper substrate as working electrode, and metallic lithium as counter-, and quasi-reference electrode (QRE). All potentials in the remainder of the text are versus the Li QRE. Dried tetraethylene glycol dimethyl ether (4G) was used as a solvent in which either 1 M LiTFSI or 1 M $LiClO_4$ electrolytes were prepared with varying amounts of added water. Figure 1 shows scanning electron microscopy images (SEM) of the lithium deposits for both salts after galvanostatic electrodeposition at -1 mA/cm^2 up to -0.74 C/cm^2 (1 µm lithium at 100% Faradaic efficiency), with concentrations of water ranging from 7.5 mM to 75 mM (135 ppm to 1350 ppm). The

figure shows that the morphology of the deposit is governed by the water concentration and that the deposition qualitatively follows the same trend irrespective of the used salt, evolving from a mossy, to a columnar morphology with increasing water concentration. The essential role of water, rather than the salt, is also apparent in the color progression of the samples, which evolves from grey/black, to blue, to yellow in both cases. As discussed later, water is in fact a prerequisite, since no deposit is obtained for the dried electrolyte. Additional (cross-sectional) SEM, AFM topography images, and potential transients are provided in Figure S1-S3.

The results in Figure 1 are in stark contrast with the prevailing explanation of HF-mediated formation of LiF being responsible for columnar growth, where LiTFSI is often used as a reference salt resistant to hydrolysis and does not yield columnar structures[16,20,25]. It is worth pointing out that we obtain these results even when using the electrolytes directly after preparation, as waiting $\gtrsim$ 48 hours is typically required after H_2O addition for the formation of HF in $LiPF_6$ based electrolytes[20,28,30]. The columnar morphologies obtained here from the LiTFSI and fluorine-free $LiClO_4$ electrolytes are therefore a key result, as it rules out such a mechanism being solely responsible for this mode of growth.

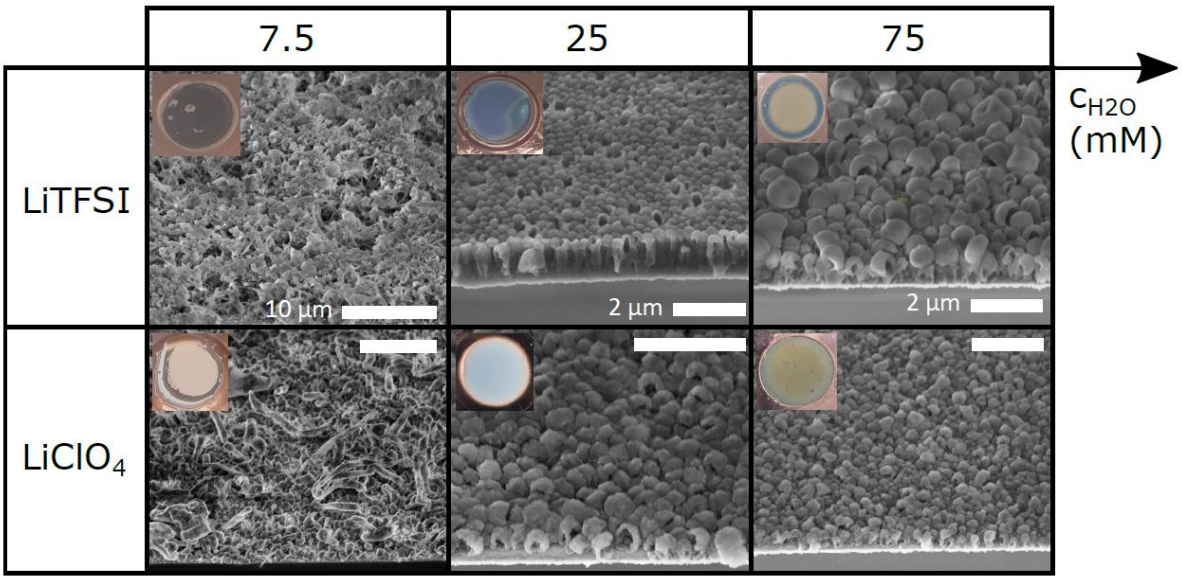

***Figure 1**: SEM images (45° sample tilt) of samples after galvanostatic electrodeposition at -1 mA/cm^2 until reaching -0.74 C/cm^2 using 1 M LiTFSI and $LiClO_4$ salts and various concentrations of the H_2O additive. Insets show digital photos of the samples. Columnar morphologies are observed for both salts, with the same progression of morphology and sample color. The scale bars are the same in both rows.*

Figure 2 shows that layers up to 30 µm (~-21.6 C/cm^2) can be grown using LiTFSI with 25 mM of H_2O at a current density of -1 mA/cm^2, and we found that columnar morphologies are obtained over a range of experimental conditions when scaling the additive concentration with the deposition current density (Figure S4). With LiTFSI, the growth proceeds at high Coulombic efficiency, where we measured a layer thickness of ~32 µm with SEM (error ~7%). As the efficiency was lower in the $LiClO_4$ electrolyte, typically resulting in black spots that wash away when rinsing (methods), we focus on LiTFSI in the remainder of this paper.

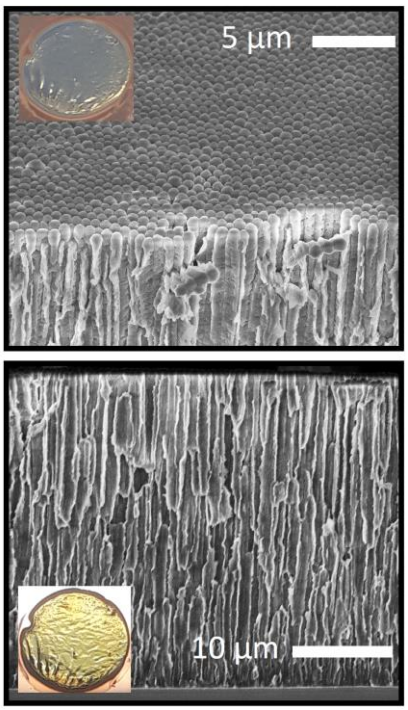

Figure 2: *SEM images of layers deposited galvanostatically from 1 M LiTFSI + 25 mM H_2O (4G) at -1 mA/cm^2 for a 30 µm layer (from ~-21.6 C/cm^2 equivalent charge). Top: 45° sample tilt. Bottom: 90° sample tilt. Insets show digital photos of the substrates at tilted (top), and perpendicular (bottom) camera angle, displaying an angular dependence of the reflection.*

Formation versus growth.

Having demonstrated that water as additive yields a similar morphology to strategies based on HF, we investigate potential mechanisms responsible for columnar growth. We independently look at the formation step (i.e. potentials without lithium deposition, U > 0 V vs. Li QRE), and the growth step (U < 0 V vs. Li QRE). In literature, both the formation step[24,25,28], and solution agitation during growth[26,31,32] (i.e. continuous supply of the additive) have been cited as factors affecting lithium morphology.

We consider the hypothesis from Kasse *et al.*[28] that the physical nanostructure, rather than chemical composition, of a surface layer formed during the formation step guides growth. Their hypothesis is based on the similarity of XPS results of samples with-, and without the

additive. To study this surface morphology the electrode was kept at potentials U > 0 V vs. Li QRE, after which the surface was characterized using *ex-situ* glovebox AFM.

Figure 3a shows linear sweep voltammograms (LSV) above 0.1 V with H_2O concentrations between 0.75 mM and 250 mM. We observed 2 peaks that *systematically* changed with the water concentration, i.e. the peak at ~1.3 V, which increases with increasing water concentration, and the peak at ~1.7 V, which increases and shifts to ~1.95 V. Based on the reaction order analysis in Figure S5, we consider 7.5 mM to be around the lower limit of our drying procedure. The behavior of both these peaks is consistent with Aurbach *et al*.[33] upon cycling, shown in Figure S6 for our system. Based on the LSV, different samples were kept at 0.1, 1.2, and 1.7 V vs. Li QRE (dash-dotted lines) in an electrolyte containing 25 mM H_2O until reaching -10 mC/cm^2, approximately the total passed charge before the onset of lithium nucleation during galvanostatic electrodeposition (Figure S3). Figure 3b shows the AFM topography images. Little to no features were observed for samples kept at 2.4 V and in the

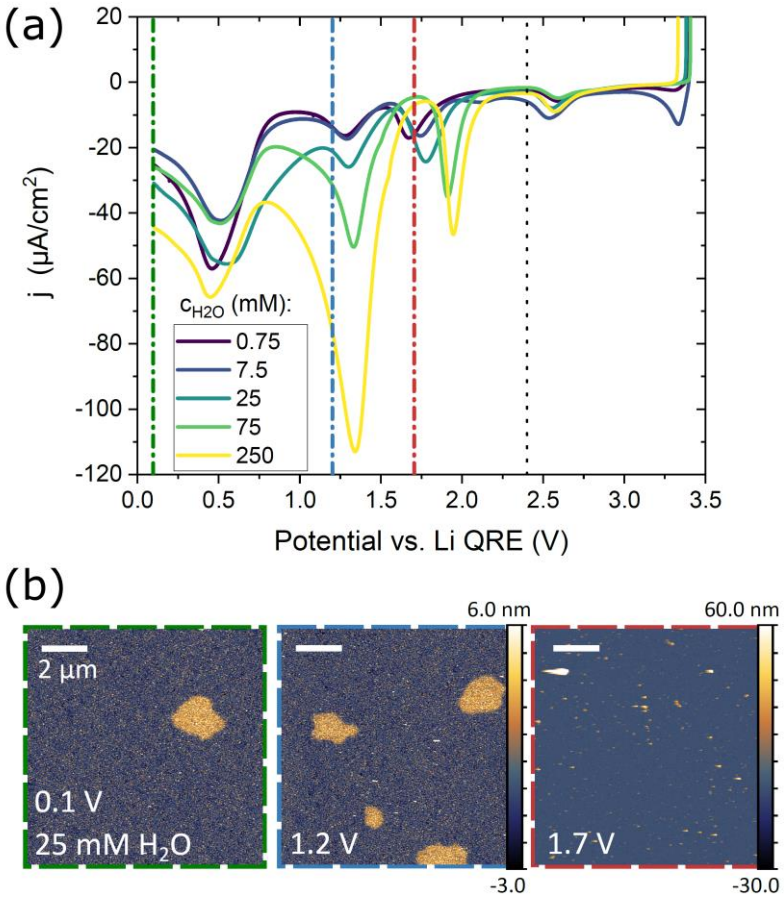

Figure 3: *(a) LSV at different concentrations of the H_2O additive from open circuit potential to 0.1 V vs. Li QRE for 1 M LiTFSI in 4G. The scan rate is 5 mV/s. Dashed lines indicate potentials where samples were prepared for ex-situ AFM (Figure S7 for the black line). (b) ex-situ AFM images of samples held at 0.1 V, 1.2 V, and 1.7 V (green, blue, red outline, respectively) for 1 M LiTFSI in 4G with 25 mM H_2O, until reaching the charge setpoint of -10 mC/cm^2. Scale bars are 2 µm.*

dried (reference) electrolyte (Figure S7). At 1.7 V the surface is seeded with particles a few tens of nm in height and ~50-100 nm in width (larger color axis). At 1.2 V and 0.1 V the most notable feature are islands of a few micron wide, but only ~3 nm high, that show a remarkable similarity to so-called 'micropancakes', typically associated with trapped gas in a liquid environment[34,35]. In particular, we observed that the density of these islands was higher for samples kept at 1.2 V in the 25 mM H_2O electrolyte ($5 \cdot 10^6/cm^2$), by more than an order of magnitude compared to samples kept at 0.1 V and the dried references (Table S1-S2). While none of these features can be linked directly to columnar deposition due to their sparsity and size, these islands appear to originate from the reduction process at 1.3 V in the presence of water.

As we did not observe a clear nanostructure responsible for columnar lithium with AFM, we replicated the experiment by Kasse *et al.*[28] to study during which part of the electrodeposition the additive plays a role. Here, we started in the electrolyte with 25 mM of H_2O additive (wet electrolyte), which was replaced with the dried electrolyte at different stages during the process. The cell was rinsed 2 times with the dried electrolyte during solvent exchange. All experiments were done galvanostatically (-1 mA/cm^2), until reaching ~-7.4 C/cm^2. Figures 4a-c show the resulting morphologies, with corresponding potential-charge traces in Figure 4d (log axis). The arrows indicate where the dried electrolyte was introduced. First, in Figure 4a only the dried electrolyte was used (green trace in Figure 4d). Notably, no adhesion between lithium and the substrate was obtained, with little material remaining after rinsing (methods). Next, formation was performed in the wet electrolyte in Figure 4b, where the dried electrolyte was introduced after the potential reached 0 V in the galvanostatic transient (at -7.2 mC/cm^2, blue trace). This enables adhesion of the deposit to the substrate, but does not result in columnar growth. Longer formation at 0 V yielded a similar mossy morphology (Figure S8). The wet formation step is therefore critical for lithium adhesion to the substrate, likely due to formation of a surface layer, but does not lead to directed growth. Finally, in Figure 4c the first -3.7 C/cm^2 was deposited in the wet electrolyte followed by -3.7 C/cm^2 in the dried electrolyte (red trace). Note that the V-|Q| traces show no noticeable difference between formation in the dried and the wet electrolytes. This experiment clearly shows that the water additive is continuously required for columnar growth, as the columnar morphology switches to non-directed growth upon solvent exchange.

Our results appear to be in contrast to those from Kasse *et al.*[28], where a columnar morphology was obtained when replacing their HF-rich LP30 electrolyte (1 M $LiPF_6$ in EC/DMC + 100 ppm HF) by the as-received electrolyte without additional HF after galvanostatic cycling to 0 V. We rationalize this difference by considering that HF formation through *in-situ* hydrolysis of $LiPF_6$ already results in smooth/columnar morphologies at trace amounts of H_2O down to 25-50 ppm[20]. In our experiments we add approximately an order of magnitude more water (25 mM H_2O ≈ 450 ppm). We therefore believe that our electrolyte system provides finer control over the process. This is strengthened by the observation that current densities in Figure 3a are a few factors smaller than those typically found for the electrochemical reduction of (100 ppm) HF[20,28,30]. Furthermore, the morphology shown in Figure 4b is very similar to the one obtained with the as-received LP30 electrolyte, without additive, in reference[28].

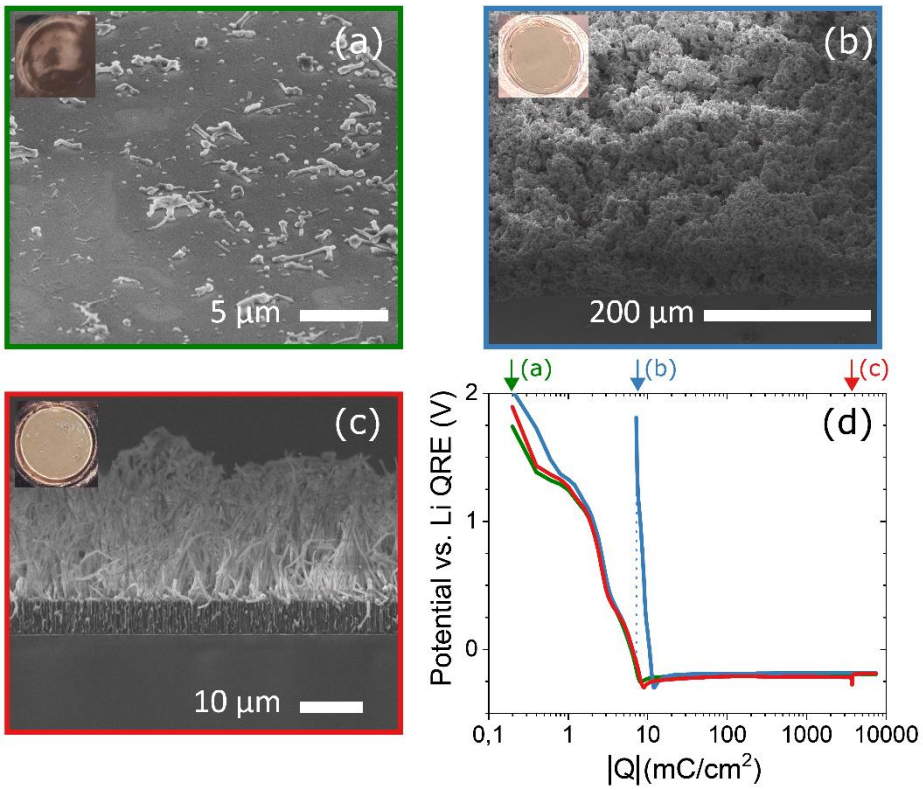

Figure 4: *(a-c) SEM images after galvanostatic deposition of -7.4 C/cm² at -1 mA/cm² from the 1 M LiTFSI in 4G electrolyte, where the wet electrolyte (+ 25 mM H_2O) is replaced by the dried electrolyte (no additive) at different total passed charge. (a-b) 45°, (c) 90° sample tilt. Insets show digital photos of the substrates. (a) Full process in the dried electrolyte results in no adhesion of lithium to the substrate. (b) Galvanostatic formation step until 0 V in the wet electrolyte (passing -7.2 mC/cm²) results in mossy growth. (c) First half of the process in the wet electrolyte (passing -3.7 C/cm²) followed by -3.7 C/cm² in the dried electrolyte results in 5 µm of columnar growth, followed by non-directed growth on top. (d) V-|Q| traces of the different protocols (log x-axis), arrows indicate where the dried electrolyte was introduced.*

Rotating Ring-Disk-Electrode

To further investigate the formation and lithium growth mechanism we used a rotating ring-disk-electrode (RRDE) with a Cu disk (A_{disk} = 0.196 cm^2) and a Pt ring electrode with a collection efficiency of N_0 = 0.256, rotated at 100 rpm. The ring potential was fixed at 3.5 V (~ 0.5 V vs. the standard hydrogen electrode), where molecular hydrogen reaching the ring is oxidized[36]. Figure 5a shows the response of the ring current as the disk potential is swept from open circuit potential (OCP) to 0.1 V at different concentrations of added water. We note that residual water after drying can be brought to the electrode through rotation (Figure S9). The disk current shows similar peaks to the stationary electrode in Figure 3a, indicating that these reactions are limited by either passivation or solid-state diffusion, rather than diffusion from the bulk (leading to a current plateau at the disk). The ring current concurrently displays peaks at ~0.5 and 1.3 V, and a smaller peak near 2 V. A $LiClO_4$ electrolyte shows similar behavior (Figure S10). The disk and the ring current increase with increasing water concentration at 1.3 V, while at 0.5 V the disk and ring peaks are highest for the dried electrolyte. To interpret the voltammogram, Figure 5b shows the fraction of the disk current resulting in hydrogen formation (direct or indirect), $\left|\frac{I_{ring}}{I_{disk}*0.256}\right|$, from OCP to 0.1 V. As this representation is sensitive to noise at low I_{disk} we consider the positions around the peaks in disk current, indicated by the arrows. As such, the first (2 V) peak appears as a dip in the fraction of hydrogen formation, corresponding to ~10% of the total current for 25 mM and 75 mM H_2O. Both the disk and the ring current show that this reaction quickly passivates, likely through formation of a surface layer. At the second (1.3 V) peak, the hydrogen fraction depends on the H_2O concentration, rising to approximately 50% at 75 mM. A striking observation is that the hydrogen fraction forms a plateau, which slowly decreases over time as the scan progresses past the 1.3 V peak. This indicates that hydrogen formation proceeds at nearly constant ratio of the disk current during this second passivation process. The absence of ring current in the reverse trace and subsequent cycles further indicates that these reactions are passivating (Figure S11). Interestingly, at 0.5 V the ring current displays a peak, while the hydrogen fraction dips before recovering to the same plateau. We therefore do not attribute this ring current peak to an additional H_2-generating reaction, but rather to a different process that enables the reaction starting near the 1.3 V peak. As the disk peak at 0.5 V is typically associated with Li underpotential deposition (UPD)[33], this can modify the surface and temporarily disturb the steady state.

Next, Figure 5c shows the electrodeposition during galvanostatic growth of ~1 µm of lithium in the 25 mM H_2O electrolyte, at -1 mA/cm^2 on the disk followed by relaxation at 0 mA/cm^2. This resulted in a blue color, similar to the stationary case (right inset). During the formation

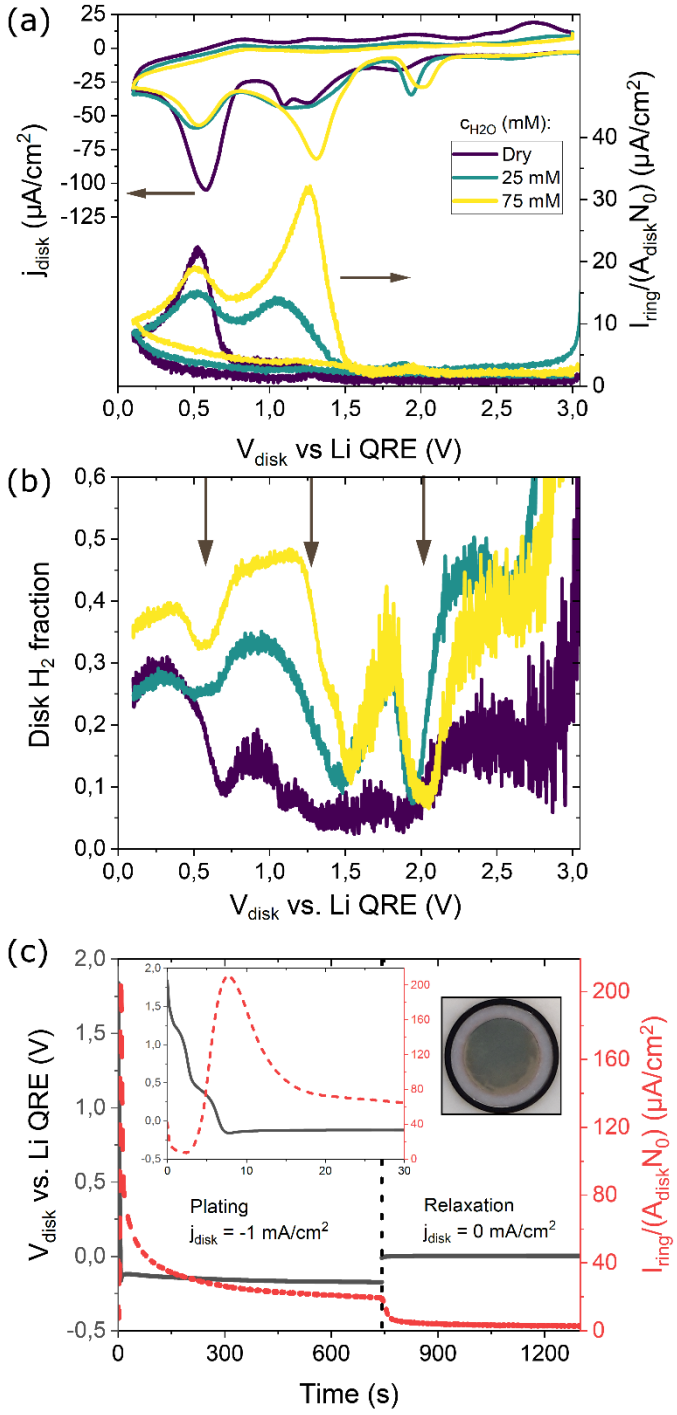

Figure 5: *(a) Cu-disk Pt-ring Rotating-Ring-Disk voltammograms with the Cu disk potential from OCP to 0.1 V and the Pt ring at 3.5 V in the 1 M LiTFSI in 4G electrolyte for different concentrations of the H_2O additive. The measured ring current was converted to the partial disk current density, $I_{ring}/(A_{disk}*N_0)$. The scan rate was 5 mV/s. (b) Fraction of the disk current generating hydrogen, $|I_{ring}/(I_{disk}*N_0)|$. The arrows indicate the peaks in disk current, taken from the 75 mM trace in (a). (c) Galvanostatic electrodeposition in the electrolyte containing 25 mM H_2O (black, left axis) on the disk at -1 mA/cm^2, with the ring at 3.5 V (red, right axis). After electrodeposition of 1 µm Li the disk current density is switched to 0 mA/cm^2, with the ring kept at 3.5 V. The left inset shows a zoom-in of the nucleation (first 30 s). The right inset shows a photo of the RRDE after the process.*

step (left inset) a small and fast decaying hydrogen signal was seen for potentials U > 1 V, followed by a steep increase with a maximum of 200 µA/cm^2 (20% of the total current) at the potential minimum, or nucleation point. During lithium electrodeposition the hydrogen partial current continuously decays down to ~20 µA/cm^2, or 2% of the total current. When the lithium deposition process is stopped the ring current rapidly decays, but a small ring current remains, which we attribute to lithium etching by water. Considering 25 mM of H_2O, this etch rate of 1-5 µA/cm^2 is small and > 1000 times less than the diffusion limit. The peak in the ring current at the nucleation implies that hydrogen generation is faster at fresh lithium, but rapidly decays as passivation layers are formed. These passivation layers are expected to (slowly) dissolve due to the water and are reformed, similar to passivation and dissolution in metal oxidation and electropolishing. Importantly, these results also indicate that hydrogen is continuously present at the interface during electrodeposition. Together with these passivation layers, a dynamic process of formation and dissolution leads to a steady state.

Following our results, a mechanism responsible for the growth of columnar lithium morphologies should (i) rely on the water additive, independent of the anion, (ii) form an adhesion layer, and act continuously during growth, (iii) involve passivation and hydrogen formation reactions. Possible reactions meeting the criteria are[37,38]:

$$2H_2O + 2Li^+ + 2e^- \rightarrow 2LiOH + H_2 \qquad U_0 = 2.09\ V\ vs.\ Li^+/Li \qquad (1)$$

$$H_2O + 2Li^+ + 2e^- \rightarrow Li_2O + H_2 \qquad U_0 = 1.68\ V \qquad (2)$$

$$2LiOH + 2Li^+ + 2e^- \rightarrow 2Li_2O + H_2 \qquad U_0 = 1.27\ V \qquad (3)$$

With standard potentials calculated from the change in free energy (Table S3). Following Figure 3 and Figure 5 the surface reactions start around 2.2 V vs. Li QRE, with a hydrogen fraction of ~10 % followed by inhibition at ~2 V, and at 1.6 V vs. Li QRE, with a hydrogen peak at 1.3 V (hydrogen fraction > 30%). The generation of hydrogen with the formation of solid LiOH and Li_2O is expected at 2.1 V and 1.7 V vs. Li^+/Li, respectively (equations 1 and 2). Additionally, the hydrogen fraction at the ~2 V reaction corresponds to -1 mC/cm^2 in the potential-hold experiments in Figure 2b. Strikingly, the volume of LiOH for this amount of charge following reaction (1) is ~0.17 µm^3, whereas the AFM images yield a similar value of 0.065 µm^3. The formation of insulating hydroxide and oxide fits with the observed passivation behavior. The hydrogen formation would then be limited by a dynamic process of hydroxide

and oxide dissolution by water and its reformation through a combination of reactions (1) to (3). Furthermore, the formation of LiH is expected in the presence of hydrogen, as was directly observed recently[8,39] (Table S3).

This hydrogen evolution reaction (HER) through reaction (1) was also argued recently for water in an ethylene carbonate solvent[40] and similarly for HF in LP30[30]. In fact, reactions (1) and (2) are remarkably similar to the electrochemical reduction of HF[20,30]:

$$2HF + 2Li^+ + 2e^- \rightarrow 2LiF + H_2 \qquad U_0 = 3.22\ V \qquad (4)$$

Due to the evident similarity of the resulting layers, we further assume (iv) that the mechanism for columnar growth is the same for our water-based process and HF-rich electrolytes. As the latter is ascribed to reaction (4), it becomes apparent that H_2 is a common denominator, which is continuously generated during growth in our system. Taken together, this leads us to believe that H_2 is an integral component for directing columnar lithium growth[41,42] in addition to the dynamic formation/dissolution of the passivation layer. For HF, we argue this is a LiH/LiF SEI coating, whereas for water it is a LiH/Li_2O/LiOH interphase[43].

Briefly, we comment here on the characteristics of the electrodeposited layers. Similar to other authors[18,20,23,26,27] we find an intriguing stripping behavior, where the columnar (shell) structure remains intact (Figure S12). This implies that stripping occurs along the length of the columns, amounting to a greatly enhanced surface area compared to the geometrical footprint. Reversible plating/stripping in such a manner therefore implies highly reduced local current densities, and mitigates issues regarding volumetric contraction/expansion of the layer.

In conclusion, we demonstrate the growth of columnar lithium layers up to 30 µm thickness, by using water as an additive. We deposit this morphology using both non-hydrolyzing (LiTFSI) and fluorine-free ($LiClO_4$) electrolytes, proving that a LiF SEI derived from HF-rich electrolytes cannot be considered as the sole structure directing component for this growth mode, as is often advocated in literature. Furthermore, we test an alternative hypothesis relying on the formation step (potentials above 0 V vs. Li QRE) and find that this is also not consistent with our results. Rather, we show that the water additive plays a continuous role in guiding the electrodeposition. Finally, we investigate the process *in-situ* using a rotating ring-disk-electrode. Based on the continuous evolution of hydrogen we propose the dynamic formation/dissolution of a LiOH, Li_2O passivation layer, accompanied by H_2 generation and

LiH formation. As hydrogen is also reported during electrochemical reduction of HF we suggest that hydrogen is an integral component for directing columnar growth, which homogenizes our results with literature on HF-based electrolytes. Considering that LiF is not the sole structure directing factor, this permits further design and control over the morphology and surface chemistry of such columnar lithium layers. We envision this to enable the use of their unique plating/stripping behavior along the length of the columns, which can potentially mitigate well-known failure mechanisms of high local current densities and large volumetric changes in lithium metal anodes.

Supporting information

Methods and experimental details, and additional SEM and AFM figures detailing columnar growth as well as additional electrochemical and RRDE data.

Acknowledgements

This work was supported by SIM (Strategic Initiative Materials in Flanders) and VLAIO (Flemish government agency Flanders Innovation and Entrepreneurship) within the SBO project "FuGels" (Grant HBC.2021.0016) in the SIM research program "SIMBA –Sustainable and Innovative Materials for Batteries.

References

1. Tikekar, M. D., Choudhury, S., Tu, Z. & Archer, L. A. Design principles for electrolytes and interfaces for stable lithium-metal batteries. *Nat. Energy* **1**, 16114 (2016).
2. Fang, C. *et al.* Quantifying inactive lithium in lithium metal batteries. *Nature* **572**, 511–515 (2019).
3. Qian, J. *et al.* High rate and stable cycling of lithium metal anode. *Nat. Commun.* **6**, 6362 (2015).
4. Oyakhire, S. T. *et al.* Electrical resistance of the current collector controls lithium morphology. *Nat. Commun.* **13**, 3986 (2022).
5. Fang, C. *et al.* Pressure-tailored lithium deposition and dissolution in lithium metal batteries. *Nat. Energy* **6**, 987–994 (2021).
6. Liu, Y. *et al.* Insight into the Critical Role of Exchange Current Density on Electrodeposition Behavior of Lithium Metal. *Adv. Sci.* **8**, 2003301 (2021).
7. Zachman, M. J., Tu, Z., Choudhury, S., Archer, L. A. & Kourkoutis, L. F. Cryo-STEM mapping of solid–liquid interfaces and dendrites in lithium-metal batteries. *Nature* **560**, 345–349 (2018).
8. Xu, G. *et al.* The Formation/Decomposition Equilibrium of LiH and its Contribution on Anode Failure in Practical Lithium Metal Batteries. *Angew. Chemie* **133**, 7849–7855 (2021).
9. Shadike, Z. *et al.* Identification of LiH and nanocrystalline LiF in the solid–electrolyte

interphase of lithium metal anodes. *Nat. Nanotechnol.* **16**, 549–554 (2021).
10. Kushima, A. *et al.* Liquid cell transmission electron microscopy observation of lithium metal growth and dissolution: Root growth, dead lithium and lithium flotsams. *Nano Energy* **32**, 271–279 (2017).
11. Yu, S.-H., Huang, X., Brock, J. D. & Abruña, H. D. Regulating Key Variables and Visualizing Lithium Dendrite Growth: An Operando X-ray Study. *J. Am. Chem. Soc.* **141**, 8441–8449 (2019).
12. Cheng, Q. *et al.* Operando and three-dimensional visualization of anion depletion and lithium growth by stimulated Raman scattering microscopy. *Nat. Commun.* **9**, 2942 (2018).
13. Chang, H. J. *et al.* Correlating Microstructural Lithium Metal Growth with Electrolyte Salt Depletion in Lithium Batteries Using 7 Li MRI. *J. Am. Chem. Soc.* **137**, 15209–15216 (2015).
14. Ko, S. *et al.* Electrode potential influences the reversibility of lithium-metal anodes. *Nat. Energy* **7**, 1217–1224 (2022).
15. Bai, P., Li, J., Brushett, F. R. & Bazant, M. Z. Transition of lithium growth mechanisms in liquid electrolytes. *Energy Environ. Sci.* **9**, 3221–3229 (2016).
16. Shi, F. *et al.* Strong texturing of lithium metal in batteries. *Proc. Natl. Acad. Sci.* **114**, 12138–12143 (2017).
17. Ding, F. *et al.* Dendrite-Free Lithium Deposition via Self-Healing Electrostatic Shield Mechanism. *J. Am. Chem. Soc.* **135**, 4450–4456 (2013).
18. Zhang, Y. *et al.* Dendrite-Free Lithium Deposition with Self-Aligned Nanorod Structure. *Nano Lett.* **14**, 6889–6896 (2014).
19. Kanamura, K., Shiraishi, S. & Takehara, Z. Electrochemical Deposition of Uniform Lithium on an Ni Substrate in a Nonaqueous Electrolyte. *J. Electrochem. Soc.* **141**, L108–L110 (1994).
20. Qian, J. *et al.* Dendrite-free Li deposition using trace-amounts of water as an electrolyte additive. *Nano Energy* **15**, 135–144 (2015).
21. Ren, X. *et al.* Guided Lithium Metal Deposition and Improved Lithium Coulombic Efficiency through Synergistic Effects of LiAsF 6 and Cyclic Carbonate Additives. *ACS Energy Lett.* **3**, 14–19 (2018).
22. Mashtalir, O., Nguyen, M., Bodoin, E., Swonger, L. & O'Brien, S. P. High-Purity Lithium Metal Films from Aqueous Mineral Solutions. *ACS Omega* **3**, 181–187 (2018).
23. Chang, W., Park, J. H., Dutta, N. S., Arnold, C. B. & Steingart, D. A. Morphological and Chemical Mapping of Columnar Lithium Metal. *Chem. Mater.* **32**, 2803–2814 (2020).
24. Zhang, X.-Q. *et al.* Columnar Lithium Metal Anodes. *Angew. Chemie* **129**, 14395–14399 (2017).
25. Chang, W., Park, J. H. & Steingart, D. A. Poor Man's Atomic Layer Deposition of LiF for Additive-Free Growth of Lithium Columns. *Nano Lett.* **18**, 7066–7074 (2018).
26. Jo, S. *et al.* The roles of nucleation and growth kinetics in determining Li metal morphology for Li metal batteries: columnar versus spherical growth. *J. Mater. Chem. A* **10**, 5520–5529 (2022).
27. He, Y. *et al.* Understanding the Relationships between Morphology, Solid Electrolyte Interphase Composition, and Coulombic Efficiency of Lithium Metal. *ACS Appl. Mater. Interfaces* **12**, 22268–22277 (2020).
28. Kasse, R. M. *et al.* Understanding additive controlled lithium morphology in lithium metal batteries. *J. Mater. Chem. A* **8**, 16960–16972 (2020).

29. Zhou, J., Chen, J., Yang, J., Nuli, Y. & Wang, J. Dendrite-Free and Micron-Columnar Li Metal Deposited from LiNO3-Based Electrolytes. *ACS Appl. Energy Mater.* **4**, 11336–11342 (2021).
30. Strmcnik, D. *et al.* Electrocatalytic transformation of HF impurity to H2 and LiF in lithium-ion batteries. *Nat. Catal.* **1**, 255–262 (2018).
31. Langenhuizen, N. P. W. The Effect of Mass Transport on Li Deposition and Dissolution. *J. Electrochem. Soc.* **145**, 3094–3099 (1998).
32. Yang, X., Wen, Z., Zhu, X. & Huang, S. Electrodeposition of lithium film under dynamic conditions and its application in all-solid-state rechargeable lithium battery. *Solid State Ionics* **176**, 1051–1055 (2005).
33. Aurbach, D., Daroux, M., Faguy, P. & Yeager, E. The electrochemistry of noble metal electrodes in aprotic organic solvents containing lithium salts. *J. Electroanal. Chem. Interfacial Electrochem.* **297**, 225–244 (1991).
34. Zhang, X. H., Zhang, X., Sun, J., Zhang, Z. & Li, G. Detection of Novel Gaseous States at the Highly Oriented Pyrolytic Graphite - Water Interface. *Langmuir* **23**, 1778–1783 (2007).
35. Seddon, J. R. T. *et al.* Dynamic Dewetting through Micropancake Growth. *Langmuir* **26**, 9640–9644 (2010).
36. Lee, H., Cho, J.-J., Kim, J. & Kim, H.-J. Comparison of Voltammetric Responses over the Cathodic Region in LiPF[sub 6] and LiBETI with and without HF. *J. Electrochem. Soc.* **152**, A1193 (2005).
37. Zhuang, G., Ross, P. N., Kong, F. & McLarnon, F. The Reaction of Clean Li Surfaces with Small Molecules in Ultrahigh Vacuum: II. Water. *J. Electrochem. Soc.* **145**, 159–164 (1998).
38. Aurbach, D. & Weissman, I. On the possibility of LiH formation on Li surfaces in wet electrolyte solutions. *Electrochem. commun.* **1**, 324–331 (1999).
39. Vilá, R. A. *et al.* LiH formation and its impact on Li batteries revealed by cryogenic electron microscopy. *Sci. Adv.* **9**, eadf3609 (2023).
40. Martins, M. *et al.* Role of Catalytic Conversions of Ethylene Carbonate, Water, and HF in Forming the Solid-Electrolyte Interphase of Li-Ion Batteries. *ACS Catal.* **13**, 9289–9301 (2023).
41. Fan, Y. W. & Wang, R. Z. Submicrometer-Sized Vaterite Tubes Formed Through Nanobubble-Templated Crystal Growth. *Adv. Mater.* **17**, 2384–2388 (2005).
42. Saadat, S. *et al.* Template free electrochemical deposition of ZnSb nanotubes for Li ion battery anodes. *Chem. Commun.* **47**, 9849 (2011).
43. Koshikawa, H. *et al.* Effects of contaminant water on coulombic efficiency of lithium deposition/dissolution reactions in tetraglyme-based electrolytes. *J. Power Sources* **350**, 73–79 (2017).